Princeton Plasma Physics Laboratory

PPPL-5445

Comparison of heat flux profile evolution during different types of edge localized modes in the National Spherical Torus Experiment

K.F. Gan, R. Maingi, J-W. Ahn, A.G. McLean, T.K. Gray, and B.D. Wirth

May 2018

Prepared for the U.S. Department of Energy under Contract DE-AC02-09CH11466.

Princeton Plasma Physics Laboratory
Report Disclaimers

Full Legal Disclaimer

Trademark Disclaimer

PPPL Report Availability

Princeton Plasma Physics Laboratory:

http://www.pppl.gov/techreports.cfm

Office of Scientific and Technical Information (OSTI):

http://www.osti.gov/scitech/

Related Links:

U.S. Department of Energy

U.S. Department of Energy Office of Science

U.S. Department of Energy Office of Fusion Energy Sciences

Comparison of heat flux profile evolution during different types of edge localized modes in the National Spherical Torus Experiment

K.F. Gan[1], R. Maingi[2], J-W. Ahn[3], A.G. McLean[4], T.K. Gray[3] and B.D. Wirth[1]

[1]*University of Tennessee, Knoxville, TN, USA*
[2] *Princeton Plasma Physics Laboratory, NJ, USA*
[3]*Oak Ridge National Laboratory, Oak Ridge, TN 37831*
[4]*Lawrence Livermore National Laboratory, Livermore, CA 94551, USA*

Abstract

In this paper, the divertor heat flux profile evolution is compared during type I, type III, and type V edge localized modes (ELMs) in the National Spherical Torus Experiment (NSTX). Small type V ELMs are routinely observed in many discharges, resulting in $\leq$ 50% transient increase in peak heat flux; as compared with true ELM-free phases in discharges, the integral power decay width(λ_{int}) is ~ 300% larger with Type V ELMs than without. During Type III ELMs, the peak heat flux can increase by up to 300% relative to the inter-ELM heat flux, and the heat profile width decreases as compared to the inter-ELM width, which is dominated by type V ELMs that routinely occur between the type III ELMs in these discharges. The peak heat flux can increase by up to 1000% during type I ELMs, with a significant contraction of the profile width. Finally analysis of the time evolution of the heat flux profiles shows instances where the peak heat flux peaks during the ELM decay phase, resulting in a very narrow profile and high PFC heating.

1. Introduction

Magnetic divertors were implemented in toroidal devices to separate the plasma facing components (PFC), where intense plasma-wall interactions (PWI) occur, from the core plasma. Thus impurities generated from PWI can be screened before they contaminate the core plasma. However X-point divertors have the downside of concentrating the plasma exhaust into narrow channels on the PFCs, resulting in high peak heat fluxes. Indeed the design[1] for the ITER with peak steady heat flux $\leq$ 10 MW/m^2 is at the limit of present heat removal technology.

The favored operational scenario for existing toroidal devices and the one intended for ITER is the high confinement or H-mode[2]; in this scenario, an edge transport barrier develops resulting in steep density, temperature, and pressure profiles. These steep profiles can destabilize local, usually ideal magnetohydrodynamic instabilities called edge localized modes (ELMs)[3, 4]. ELMs cause a rapid, periodic ejection of edge plasma stored energy which can transiently increase the steady divertor heat flux by ten-fold or more[5]. ELMs are thought to be caused by violating either pressure gradient and/or edge current/gradient limits, i.e. peeling-ballooning modes[6-8], which result in coherent, intermediate wavelength, instabilities. These instabilities evolve with a linear growth in time, followed by a non-linear growth phase[9]. During the non-linear growth phase, helical filamentary structures aligned with the magnetic field topology expand radially from the edge plasma onto the open field lines of the scrape-off layer[10-12]. These filaments result in multiple heat and particle flux helical "stripes" in the divertor[13]. Understanding the structure of these filaments on the divertor PFCs is crucial for predictive capability of the transient divertor heat flux profile for ITER and other devices.

The filamentary structure of power deposition is also important since it can significantly increase the plasma wetted area during ELMs. In the JET device, filamentary structures were easily resolved by an IR imaging system with 1.7mm spatial resolution and ~ 100 μsec time resolution[14]. In that work, it was shown that the heat flux due to the ELM increased rapidly with a characteristic time scale τ_{IR}, after

which it slowly decayed. There τ_{IR} was defined as the duration of the power deposition increase from 10% above initial value to 100% of the maximum measured value[15]. It was also found that the number of filaments increased in the first 40% of τ_{IR}, and then remained constant until τ_{IR}[14].

In this paper, we report analysis of the heat flux during and after various ELM types[16, 17] observed in the National Spherical Torus experiment (NSTX)[18]: large Type I ELMs, intermediate type III ELMs, and small type V ELMs. Studies from other devices have shown that ELMs increase the plasma wetted area[19, 20]. Here we will show that the heat flux profile width changed only modestly during type V ELMs but contracted during type I and type III ELMs; this is attributed to the routine occurrence of type V ELMs between these other ELM types. When compared with true ELM-free H-mode, the footprint indeed grows wider during type I and type III ELMs. In addition, we will describe the heat flux temporal evolution in terms of τ_{IR}.

There is broad interest in small ELM regimes for ITER. In this paper, we report the heat flux characteristics of type V ELMs specifically and small ELMs in general for the first time. For reference we note that type V ELMs are single or double filamentary perturbations resulting in ≤1% plasma stored energy loss per event, in a wide variety of shapes and with $\beta_p \geq 0.5$[21, 22]. We found that type V ELMs increase the integral power width(λ_{int}), where $\lambda_{int} = P_{div}^{out} / (2\pi R_{peak}^{div,out} q_{peak}^{div,out} f_x)$[23]. Here P_{div}^{out} is the integrated outer divertor power, $R_{peak}^{div,out}$ is the radial location of the peak heat flux, $q_{peak}^{div,out}$, f_x is the magnetic flux expansion. Furthermore we found that the type V ELMs actually reduce the q_{peak} as compared to true ELM-free phases.

The remainder of this paper is organized as follows: the NSTX device and the IR diagnostics used for the temperature measurements and heat flux calculations are presented in section 2. In section 3, the relationship between λ_{int} and q_{peak} for different types of ELMs is described. In section 4, we describe the detailed time evolution of power deposition and peak heat flux during individual ELMs. Finally, the paper concludes with a brief summary of the results in section 5.

2. Diagnostic setup and analysis tools

A Santa Barbara Focal plane (SBF161) Infrared (IR) camera was used to measure the lower divertor temperature evolution on the divertor PFCs[24] . The field of view of the IR camera can be varied with a mirror, as shown in Figure 1. The camera is sensitive to IR radiation between 2-12 μm. The detector has 128×128 pixels, which give a 5.8mm spatial resolution at the divetor PFCs. The frame rate can be changed by altering the frame size: 1.6 kHz for full frame and 6.3kHz for 96×32 pixels. The IR camera can measure a 2D toroidal-radial temperature distribution. In this paper, we focus on outer plate divertor heat flux because the inner strike points are out of the field of view for most of shots; early experiments showed that the maximum heat flux up to 10 MW/m^2 occurs near the outer divertor strike point in NSTX[25].

The divertor heat flux profile was calculated from the calibrated surface temperature from the IR camera. The divertor heat fluxes were computed using the 3-D heat transfer code, TACO[26, 27]. The TACO code was upgraded[28] to allow inclusion of a surface film in poor thermal contact with the underlying PFC substrate, using the same technique as in the 2-D THEODOR code[29]. Specifically an effective heat transmission coefficient through a thin surface film is used: $\alpha = \kappa_{layer}/\delta_{layer}$, where the latter two quantities represent layer thermal conductivity and thickness respectively[30]. Because the thermal characteristics and thickness of the layer are unknown, the value of α is often chosen to avoid having a negative heat flux following ELMs. In NSTX, the simple criterion used in this work determined the α value needed to keep energy deposition constant after the end of the discharge[28], since there is no power going to the divertor after the end of discharge. Typical α values of 60-100 kW/m^2-K were needed for NSTX discharges, rather close to the 100 kW/m^2-K reported in ASDEX-Upgrade[30]. In addition, the results of the TACO code with this modification gave nearly identical results to the THEODOR calculation applied to NSTX[28].

3. ELM heat deposition patterns

All of the discharges analyzed in this paper were lower single-null discharges,

with varying degrees of δ_r^{sep}, which is the radial separation between the two X-points mapped to the outer midplane. In addition, these discharges were obtained with boronized walls, prior to the usage of lithium coatings in this particular campaign (lithium coatings are known to alter the surface emissivity relative to graphite PFCs). We first discuss results for small type V ELMs, followed by medium type III ELMs, and finally large type I ELMs. The shots analyzed in this paper are listed in table 1.

Shot #	Time (s)	Type	Ip(MA)	$n_e(10^{19}/m^3)$	P_{NBI}
132403	0.43-0.47s	Type v ELM	0.6	4.4-4.9	3.2MW
132406	0.21-0.24s,	Tye v ELM	0.6	2.6-3.2	5.2MW
132401	0.17-0.55s	Type III /Type v ELM	0.6	2-5	4MW
132460	0.23-0.4s	Type III ELM	0.7	3.3-4.3	2MW
132438	0.19-0.27s	Type I ELM	0.8	3.1-4.7	6MW

3.1. Type V ELMs

NSTX has observed a high performance operating regime with small ELMs that were labeled as "type V" because they differ from other existing ELM types[21, 22]. Type V ELMs have a single or double filamentary structure that originates usually in the lower part of the H-mode pedestal where $T_e < 150$ eV. There is limited evidence for a continuous edge-localized instability in certain type V ELM discharges[31]. An example of a type V ELM discharge is shown in Figure 2, from t~0.43 sec (see the red vertical line). There is a rollover in the plasma stored energy at t~ 0.4 sec, which corresponds to the growth of MHD activity and/or increase in core radiated power. Note that the Dα signal increase is less than 50% of the baseline value during type V ELMs. The Dα signal is irregular during type V ELMs; hence it is difficult to compute a regular frequency. For reference, the frame rate of IR data for shot #132403 is 6.3kHz, which is well above the approximate type V ELM "frequency" that is typically between 0.5 and 1 kHz.

Figure 3 displays the effect of type V ELMs on the divertor heat flux profiles. Panel 3a shows a contour plot of heat flux as a function of radius and time from #132403; about a dozen type V ELMs are visibly spreading out the heat flux footprint relative to the inter-ELM profile. Panel 3b shows that each type V ELM increases peak outer divertor heat flux $q_{peak}^{div,out}$ by ~ 20%, although certain events can increase $q_{peak}^{div,out}$ by ~ 50% . Panel 3c shows the time evolution of the heat flux profile during the ELM. For theis example of type V ELMs, it is clear that the main additional heat flux occurs in a zone displaced by ~ 0.05m relative to the original outer strike point, i.e. the profile indeed broadens with the ELM heat flux. There is energy deposition near the strike points with a similar heat flux profile superimposed by an additional contribution out of the strike points during ELM. We note that the ELM heat flux profiles show multiple peaks during the type V ELM.

Figure 4 contrasts the heat flux profiles during type V ELMs with an ELM-free phase observed after the L-H transition . After the L-H transition, the $q_{peak}^{div,out}$ increased by ~ 300%, mostly due to a shrinking of λ_{int} by 67%. Hence the power deposition remained constant in that ELM-free phase. Type V ELMs were first observed at t ~ 0.21 sec when the filamentary heat load appears on the target and the power deposition increase instantly, after which λ_{int} increased slowly and $q_{peak}^{div,out}$ decreased, again at constant power deposition. As also shown in Figure 3, type V ELMs reduced the $q_{peak}^{div,out}$, by increasing the extra heat flux in a spatial region separated from the strike points. It was also found the λ_{int} increased with increasing plasma density.

3.2 Type III ELMs

Type III ELMs are medium sized ELMs that result in a few % drop in the plasma stored energy and are typically obtained when the auxiliary heating power is close to the L-H power threshold[4, 32]. The frequency of Type III ELMs decreases with increasing auxiliary heating power; a small window of ELM-free H-mode is sometimes obtained before the observation of large, Type I ELMs. In NSTX, the operating window between Type III and Type I ELMs can be quite narrow[33], although

the window for type III ELM operation can be substantial at low I_p, in terms of auxiliary heating power. The temporal evolution of two different type III ELM discharges from NSTX is shown in Figure 5. These two discharges have moderate differences in I_p and in plasma shaping, and a more substantial difference in NBI power and β_p.

Figure 6 and Figure 7 show the heat flux evolution from several type III ELMs from the two discharges shown in Figure 5. Panel 6(a) shows the evolution of the heat flux profile as a function of time. Panel 6(b) shows that λ_{int} decreased by 50% as the $q_{peak}^{div,out}$ increased from the ELM energy pulse. However the λ_{int} rebuilt slowly between type III ELMs to a nominal value ~0.03m, i.e. panel 6(c) at 264.928ms. The first ELM filament in panel 6(c) appeared at t=265.087 msec; this filament increased the heat flux ~ -0.08m away from the nominal outer strike point prior to the ELM onset. Following this, the peak heat flux reverted back to the strike point, resulting in a narrow λ_{int} ~0.015m, i.e. nearly 50% smaller than the pre-ELM heat flux profile. Panels 7(a)-(c) show the corresponding evolution for the second type III ELM discharge. Here the filamentary deposition of the heat flux was distributed wider at t=273.597 msec, actually increasing λ_{int} during the type III ELM. Then, during the ELM recovery phase, the profile reverted slowly to a peak near the strike point, resulting in a reduction of λ_{int} to ~ 0.02m. The difference in these two discharges is the time scale for profile reversion back to the strike point area: this process took longer in the lower set of panels, resulting in a peak heat flux that occurred during the first ELM filament peak, where the λ_{int} is largest during ELMs. The different behavior between the λ_{int} and the $q_{peak}^{div,out}$ in these two discharges is also shown in Figure 8.

Some individual ELM-like filaments can be seen between type III ELMs for the shot 132401; inspection of those filament with the gas-puff imaging diagnostic [34,35] indicate these filaments between type III ELMs are actually type V ELMs[21]. In addition, type V ELMs are present in the figure 6(a)from #132401, the heat flux at inter-ELM during 0.267-0.27s is multiplied by 2. Previously a $\beta_p \geq 0.6$ threshold was identified for the onset of type V ELMs[22]; here $\beta_p=4\mu_0 W_{MHD}/(3|B_{pol}|^2)$ where W_{MHD} is

the plasma stored energy from equilibrium reconstructions[36,37], μ_0 is the permeability of free space, and $|B_{pol}|$ is the flux-surface averaged magnitude of the poloidal magnetic field at the separatrix. Indeed the β_p value is higher for #132401than #132460 (because of the higher P_{NBI} and lower I_p), suggesting a continuous relationship between the effectiveness of type V ELMs in spreading the heat flux profile between the type III ELMs. Previous studies have shown very broad heat flux profiles at high β_p in other tokamaks, independent of the ELM type[38].

3.3 Type I ELMs

Type I ELMs are thought to occur when the edge plasma violates ideal MHD limits for current-driven kink/peeling modes and/or pressure gradient driven ballooning modes[6-8]. In contrast to Type III ELMs the observed frequency of type I ELMs increases with heating power. These large ELMs can result in up to a 10% drop in the plasma stored energy per event, resulting in high transient heat loads.[3, 5, 39-41]

Type I ELMs are also routinely observed in NSTX discharges; the example in this paper come from a high X-point, low elongation scenario developed for small ELM similarity experiments[33]. Figure 8 shows the temporal evolution of a discharge with ordinary type I ELMs; Figure 8(b) shows that these ELMs resulted in discrete drops of the plasma density and in discrete Dα emission spikes in panel 8(c). The energy loss per ELM relative to the plasma stored energy was in the 2-9% range. This particular scenario uses a large separation between the X-point and lower divertor PFCs, resulting in very low poloidal flux expansion values, f_x, of 1.5-2 relative to the outer midplane. More typical values of f_x in NSTX range from 5-30. Because the (divertor-mapped) midplane width of the heat flux profile is approximately constant[42], the low value of f_x results in small power deposition width at the divertor, and consequently high $q_{peak}^{div,out}$.

The evolution of the heat flux profile for the Type I ELMy discharge is shown in Figure 9. Panel 9(b) shows that that the $q_{peak}^{div,out}$ increased by up to 1000% during each ELM, with a 33% decrease in the λ_{int}. Owing to the low flux expansion, the ELM filaments (e.g. at t=266.496 msec in panel 9(c)) increase the peak heat flux

within a couple of cm of the original strike point.

It is unclear if the midplane-mapped target heat flux profiles during ELMs have physical significance, because of the probable change to the magnetic topology itself for the large ELMs. It can be seen that the heat flux profile contracted during the type I ELMs (# 132438) and the type III ELMs (# 132401), but when compared with true ELM-free H-mode, the footprint indeed grew wider during type I and type III ELMs.

4. Profile evolution during ELM rise and decay time

The ELM energy pulse to divertor target can be separated into two phases with a characteristic timescale τ_{IR}, which was previously defined as the length of time it took for the power deposition to increase from 10% above its initial value to 100% of the maximum measured value[15]. In this picture the divertor PFC temperature peaks at τ_{IR}. The maximum target temperature during ELMs is decided by the maximum heat flux, not the peak power deposition. The maximum q_{peak} appears at τ_{IR} which make the peak temperature at τ_{IR}. The maximum q_{peak} rise during ELMs follows this pattern for many ELMs in NSTX. However we also observe instances where the q_{peak} occurs after the time of peak power deposition; this occurs in the ELMs where the peak heat flux peaks after the time of peak power deposition.

Figure 11(a)-(b) shows 10 ELMs of 12 ELMs when the maximum power deposition was aligned at the onset of the ELM filaments, but the maximum heat flux followed the ELM filaments later and appeared at ELM decay time. Panels 0(c)-(d) show the 12 ELMs cases where the maximum power deposition and heat flux were all aligned with the onset of ELM filaments. This two difference ELMs behavior are from two discharges, the first one is #132401, the later one is #132460. The parameter for this two discharges is shown in Figure 5. The shot 132401 has higher NBI power and plasma stored energy compared to the shot 132460. In panels 11 (a), the heat flux during the onset of ELM filaments was distributed farther from the outer strike point, which is also shown in Figure 6. Although there are two ELMs are this case where the maximum power deposition and heat flux were all aligned with the onset of ELM filaments, the heat flux at outer strike point still was not maximum value at the ELM filaments and would increase after the peak power deposition,

which is the same as the other 10 ELMs.

The maximum heat flux appears during ELM decay time also happens in large ELM, as shown in panel 12 (a)-(b). The peak power deposition 5MW versus 13MW/m^2 q_{peak} at the onset of ELM filament, the maximum heat flux 26MW/m^2 appeared during ELM decay time, which is two times larger than the q_{peak} at the ELM filaments. The power deposition at maximum heat flux is 4.5MW which is close to the maximum power deposition at ELM filament. The heat flux distribution is wide at ELM filaments, the λ_{int} decrease fast after the ELM filament, which is can be seen in Figure 6, more power deposited on target during ELM decay time will increase the q_{peak} fast. This latter phenomenology would be of obvious concern to future devices. A slight variation to these two patterns, which is rare in NSTX, is shown in panels 02 (c)-(d), where the ELM filaments arrived before the time of peak power deposition; in this case, the peak heat flux and temperature rise were aligned with the peak power deposition time, but the heat flux footprint was very narrow. This situation makes more ELM power deposit on target after the ELM filaments. The q_{peak} at peak power deposition is 9.5MW/m^2, which is ~3 times larger than the q_{peak} at ELM filament. The reason for the temporal misalignment between the peak power deposition and the maximum peak heat flux is not understood. We assume two channel transport mechanism to explain this phenomenon. There is a fast channel transporting the overwhelming amount of energy during the ELM remote from the strike points, cause the filamentary structure on divertor with large λ_{int}. Another slow channel is same energy transport channel as in turely ELM free phase with narrow λ_{int}, which deposits the energy slightly later compare with first channel. If large energy transport with slow channel, it may cause the ELM peak heat flux appear at ELM decay time.

5. Summary and Conclusions

In this paper, we showed the first analysis of the evolution of heat flux profiles

during various ELMs in NSTX. The small, type V ELMs caused a $\leq$ 20% increase in $q_{peak}^{div,out}$; as compared to a true ELM-free phase, however, the $q_{peak}^{div,out}$ actually decreased and the λ_{int} increased, the latter by up to 300%. It was observed that $q_{peak}^{div,out}$ decreased with increasing density. For Type III ELMs we found that λ_{int} decreased by up to ~50% with increasing $q_{peak}^{div,out}$; the "inter-ELM" phases for those discharges were dominated by type V ELMs. Type I ELMs showed the largest transient increase in $q_{peak}^{div,out}$ (up to 1000% in low flux expansion discharges), with a ~33% contraction of λ_{int}.

We also evaluated the evolution of the peak power deposition, peak heat flux, and during the ELM rise and decay time. Here it was found that many ELMs showed a temporal alignment of the peak power deposition and maximumpeak heat flux., as reported in other devices[14, 15]. However a significant number of ELMs exhibited a different evolution: the peak heat flux occurred after peak power deposition in the ELM decay phase, with a very narrow footprint. Additional research is needed to identify the mechanism(s) for this latter phenomenology, which could lead to unacceptably high PFC thermal excursions if they were to occur in future devices.

ACKNOWLEDGMENTS

This work was supported by the U.S. Department of Energy, contract Nos. DE-AC05-00OR22725 and DE-AC02-09CH11466. We thank A. Herrmann and IPP-Garching for use of the THEODOR heat conduction code, and A. Kirk and CCFE-Culham for use of the TACO code. The first author was supported by an exchange program between the Institute of Plasma Physics, the Chinese Academy of Sciences, and the Princeton Plasma Physics Laboratory.

Figure Captions

1. (a) Photograph of the NSTX lower divertor region, with the IR field of view shown by the red shaded region, and (b) plasma reconstructed equilibrium and radial field-of-view of the fast IR diagnostic.
2. Example of type V ELM discharge ($t \geq 0.43$ sec): (a) I_p and P_{NBI}(MW), (b) line-averaged density n_e, (c) upper divertor Dα emission, (d) plasma stored energy from equilibrium reconstructions and β_p, (e) odd-N MHD activity, (f) main chamber radiated power, and (g) position of the outer divertor strike point. The vertical red line represents the time when type V ELMs began to appear.
3. Heat flux data during type V ELM: (a) contour plot of the heat flux profile as a function of radius and time, (b) the evolution of λ_{int} and $q_{peak}^{div,out}$, (c) evolution of the profile in sequential time slices during a Type V ELM.
4. Comparison of heat flux profile during type V ELMs and the ELM-free phase following the L-H transition: (a) contour plot of the heat flux profile as a function of radius and time, (b) the relationship between λ_{int} and $q_{peak}^{div,out}$, and integrated power deposition during type V ELMs, along with evolution of the density.
5. Example of type III ELM discharges: (a) plasma current I_p, (b) neutral beam heating power P_{NBI}, (c) line-averaged density n_e, (d) divertor Dα emission, (e) β_p, (f) plasma stored energy from equilibrium reconstructions, (g) main chamber radiated powerand (h) position of the outer divertor strike point.
6. Heat flux characteristic during type III ELMy discharges are from #132401: (a) contour plot of the heat flux profile as a function of radius and time; (b) the evolution of $\lambda_{int}$and $q_{peak}^{div,out}$; (c) evolution of the profile in sequential time slices during a Type III ELM.
7. Heat flux characteristic during type III ELMy discharges are from #132460: (a) contour plot of the heat flux profile as a function of radius and time; (b) the evolution of λ_{int} and $q_{peak}^{div,out}$; (c) evolution of the profile in sequential time slices during a Type III ELM.
8. The evolution of λ_{int} and $q_{peak}^{div,out}$ of the shot 132460 (a) and 132401 (b).
9. Example of type I ELM discharge: (a) plasma current I_p and neutral beam heating power P_{NBI}, (b) line-averaged density n_e, (c) divertor Dα emission, (d) plasma stored energy from equilibrium reconstructions and β_p, (e) odd-N MHD activity, (f) main chamber radiated power, and (g) position of the outer divertor strike point .
10. Heat flux data during type I ELMs: (a) contour plot of the heat flux profile as a function of radius and time, (b) the evolution of λ_{int} and $q_{peak}^{div,out}$, (c) evolution of the profile in sequential time slices during a Type I ELM.
11. Evolution of the ELM heat flux for dozens of ELMs cases. In panels (a)-(b), the maximum heat flux and power deposition occurred at the onset of ELM filaments at the target. In panels (c)-(d), the maximum heat flux occurred after ELM filaments at the target for most of ELMs. 12. Evolution of the ELM heat flux of the shot 132406. In panels (a)-(b), the maximum heat flux occurred after

ELM filaments for the large ELM, In panels (c)-(d), the maximum heat flux and power deposition occurred after ELM filaments at the target.

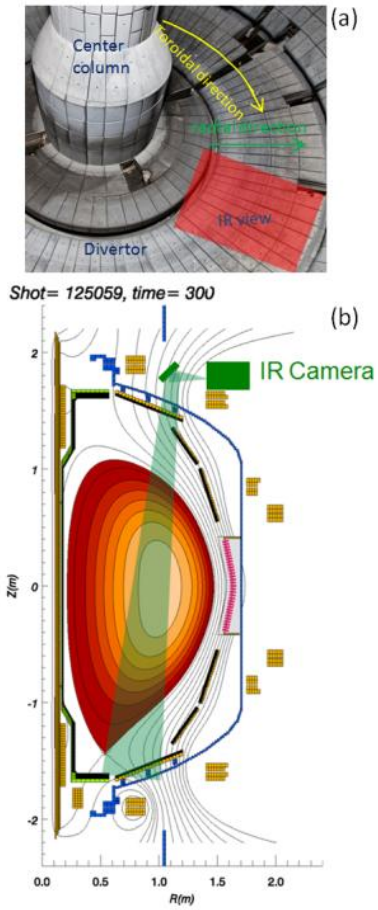
(a)
Center column
Toroidal direction
IR view
Divertor
Shot= 125059, time= 300
(b)
IR Camera
Z(m)
R(m)
0.0
0.5
1.0
1.5
2.0
2
1
0
-1
-2

Figure 1

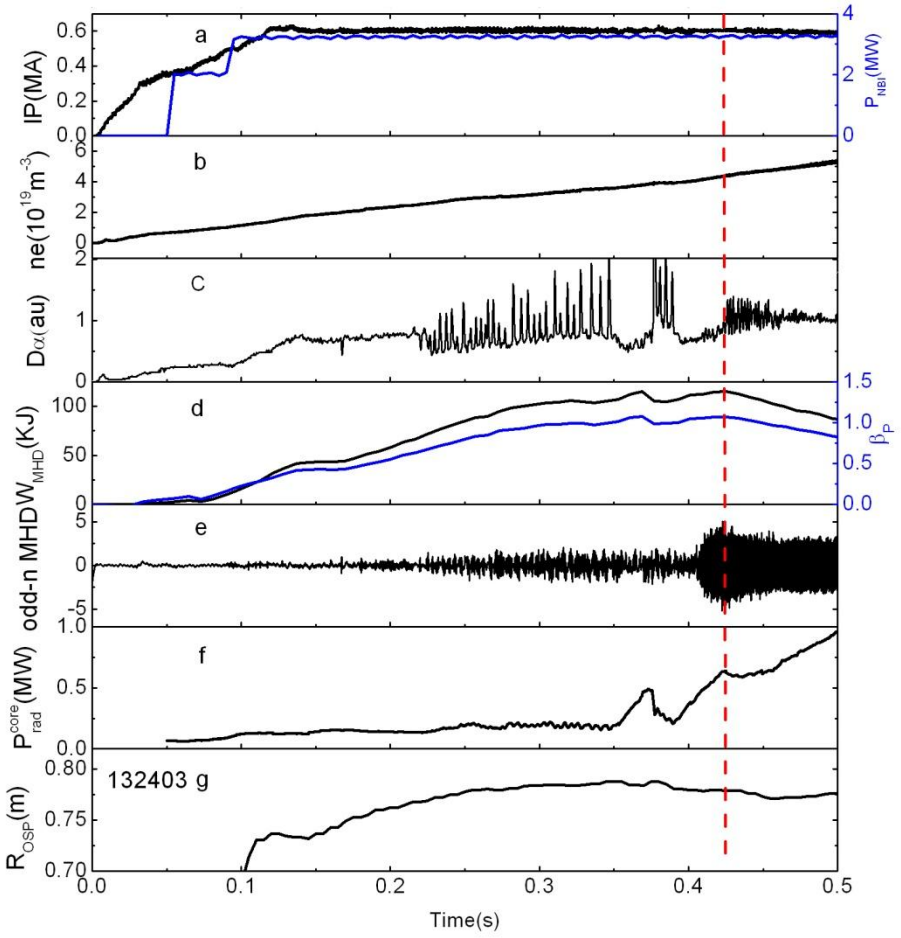
a
IP(MA)
P_{NBI}(MW)
b
ne($10^{19}$$m^{-3}$)
C
Dα(au)
d
W_{MHD}(KJ)
β_P
e
odd-n MHD
f
P_{rad}^{core}(MW)
132403 g
R_{OSP}(m)
Time(s)

Figure 2

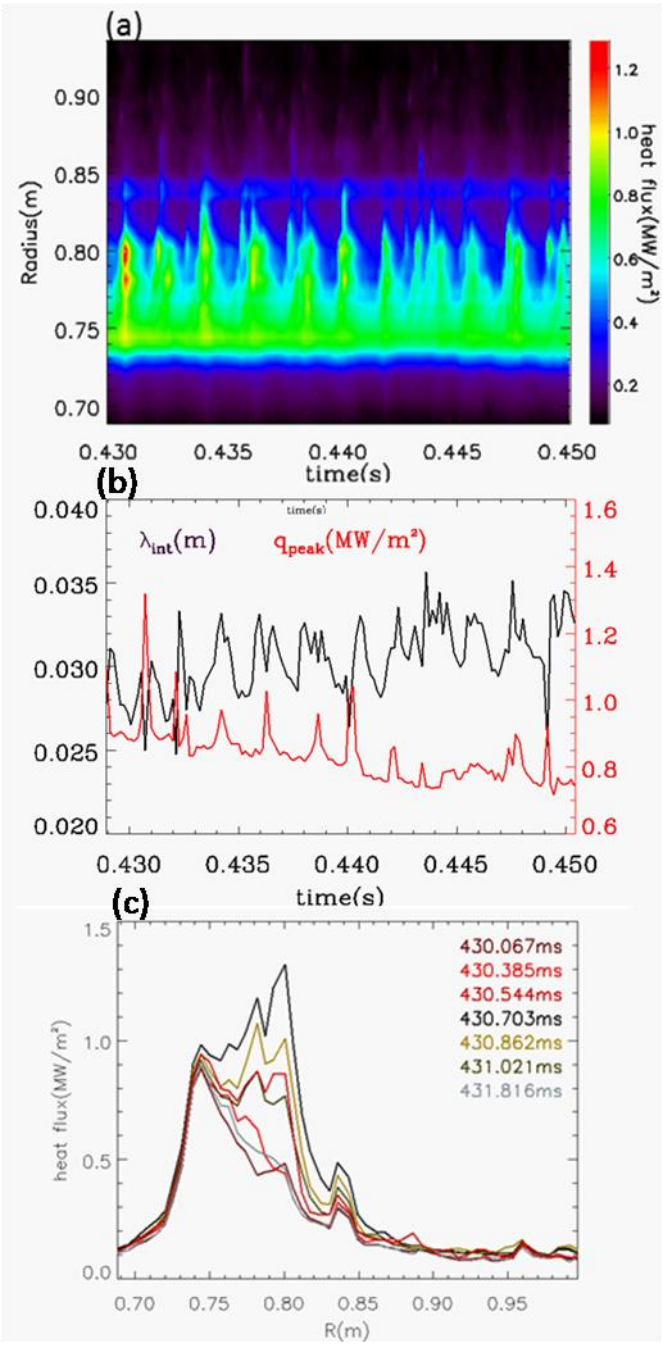
(a)
Radius(m)
0.90
0.85
0.80
0.75
0.70
0.430
0.435
0.440
0.445
0.450
time(s)
heat flux(MW/m²)
1.2
1.0
0.8
0.6
0.4
0.2
(b)
λ_{int}(m)
q_{peak}(MW/m²)
0.040
0.035
0.030
0.025
0.020
1.6
1.4
1.2
1.0
0.8
0.6
0.430
0.435
0.440
0.445
0.450
time(s)
(c)
heat flux(MW/m²)
1.5
1.0
0.5
0.0
0.70
0.75
0.80
0.85
0.90
0.95
R(m)
430.067ms
430.385ms
430.544ms
430.703ms
430.862ms
431.021ms
431.816ms

Figure 3

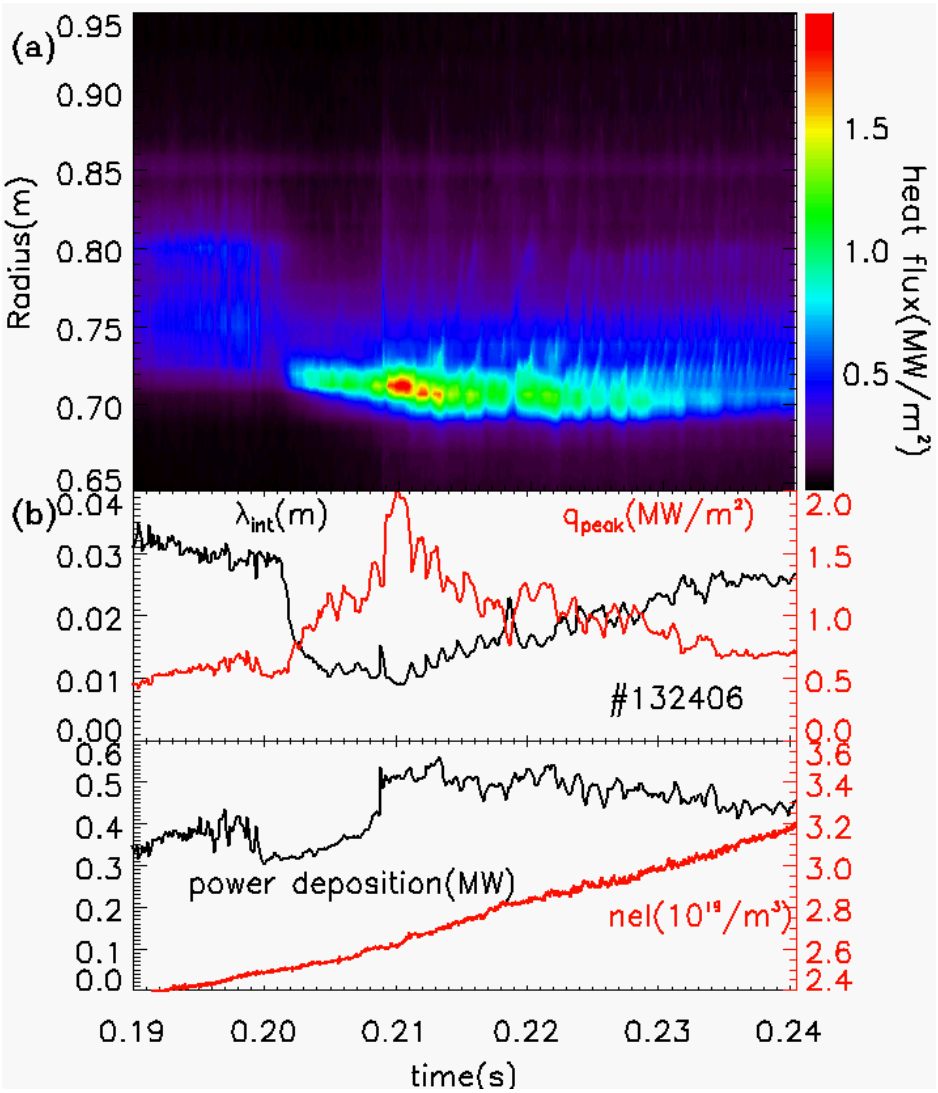
(a)
Radius(m)
0.95
0.90
0.85
0.80
0.75
0.70
0.65
1.5
1.0
0.5
heat flux(MW/m²)
(b)
λint(m)
qpeak(MW/m²)
0.04
0.03
0.02
0.01
0.00
2.0
1.5
1.0
0.5
0.0
#132406
0.6
0.5
0.4
0.3
0.2
0.1
0.0
3.6
3.4
3.2
3.0
2.8
2.6
2.4
power deposition(MW)
nel(10¹⁹/m³)
0.19
0.20
0.21
0.22
0.23
0.24
time(s)

Figure 4

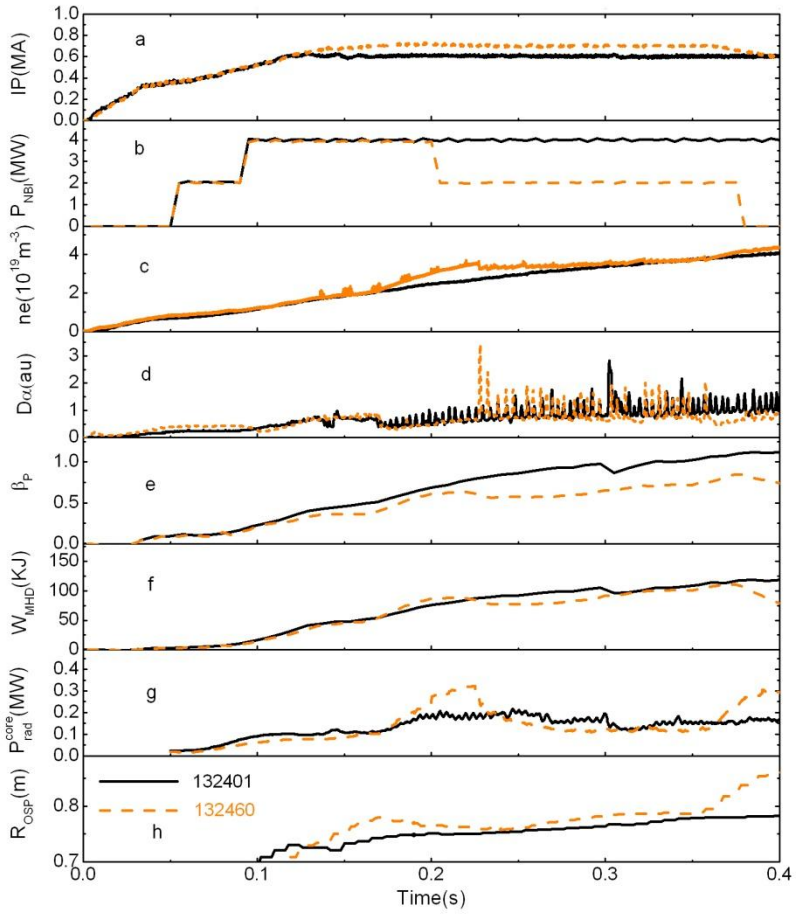
IP(MA)
a
P_{NBI}(MW)
b
ne($10^{19}$$m^{-3}$)
c
Dα(au)
d
β_P
e
W_{MHD}(KJ)
f
P_{rad}^{core}(MW)
g
R_{OSP}(m)
132401
132460
h
Time(s)

Figure 5

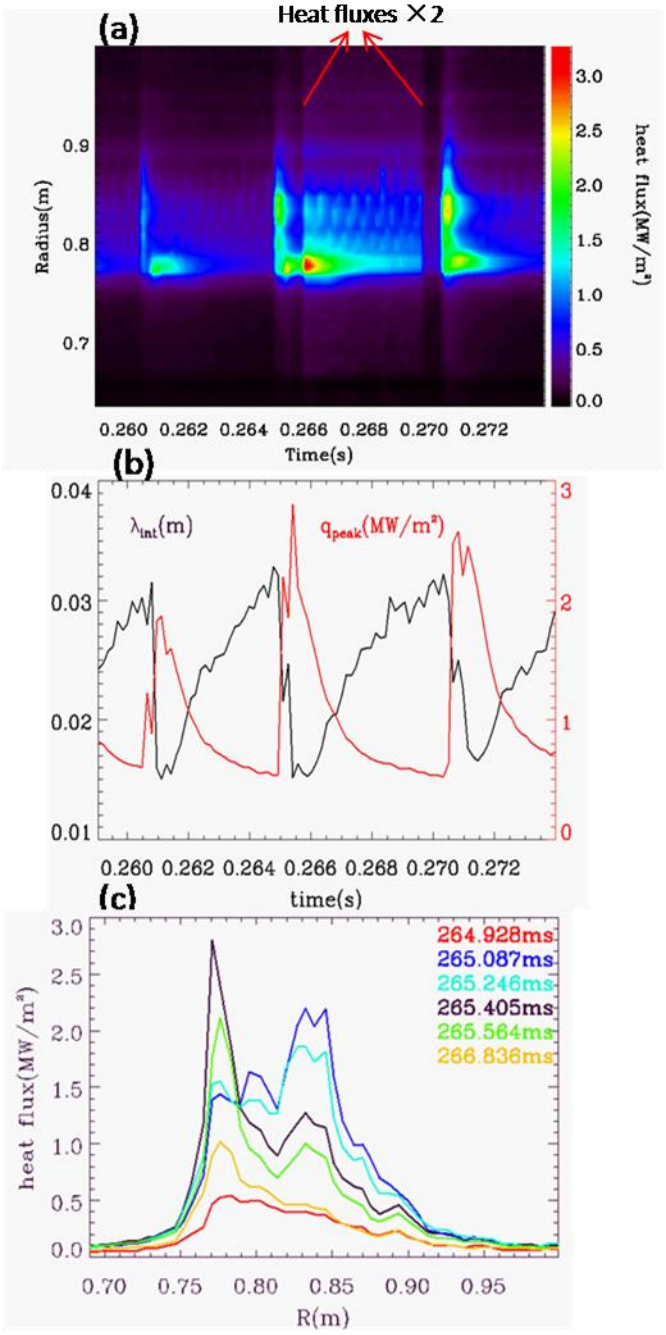
(a)
Heat fluxes ×2
Radius(m)
0.9
0.8
0.7
heat flux(MW/m²)
3.0
2.5
2.0
1.5
1.0
0.5
0.0
0.260 0.262 0.264 0.266 0.268 0.270 0.272
Time(s)
(b)
λint(m)
qpeak(MW/m²)
0.04
0.03
0.02
0.01
3
2
1
0
0.260 0.262 0.264 0.266 0.268 0.270 0.272
time(s)
(c)
heat flux(MW/m²)
264.928ms
265.087ms
265.246ms
265.405ms
265.564ms
266.836ms
3.0
2.5
2.0
1.5
1.0
0.5
0.0
0.70 0.75 0.80 0.85 0.90 0.95
R(m)

Figure 6

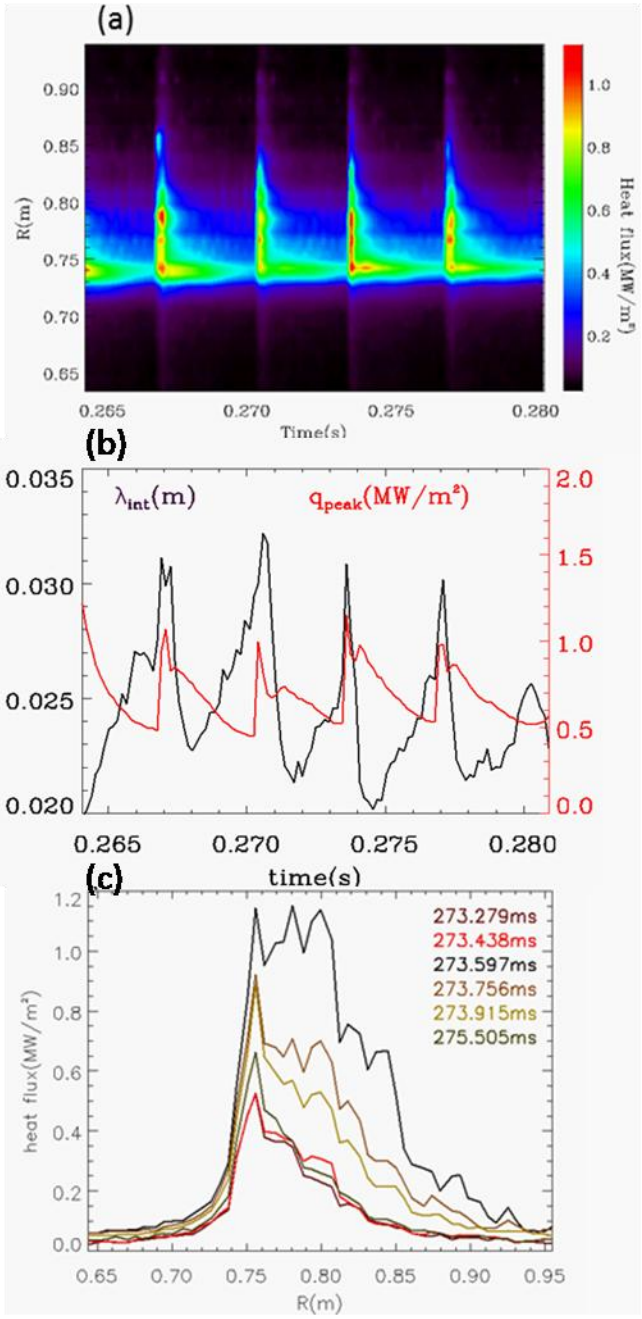
(a)
R(m)
Time(s)
Heat flux(MW/m²)
(b)
λint(m)
qpeak(MW/m²)
time(s)
(c)
heat flux(MW/m²)
R(m)
273.279ms
273.438ms
273.597ms
273.756ms
273.915ms
275.505ms

Figure 7

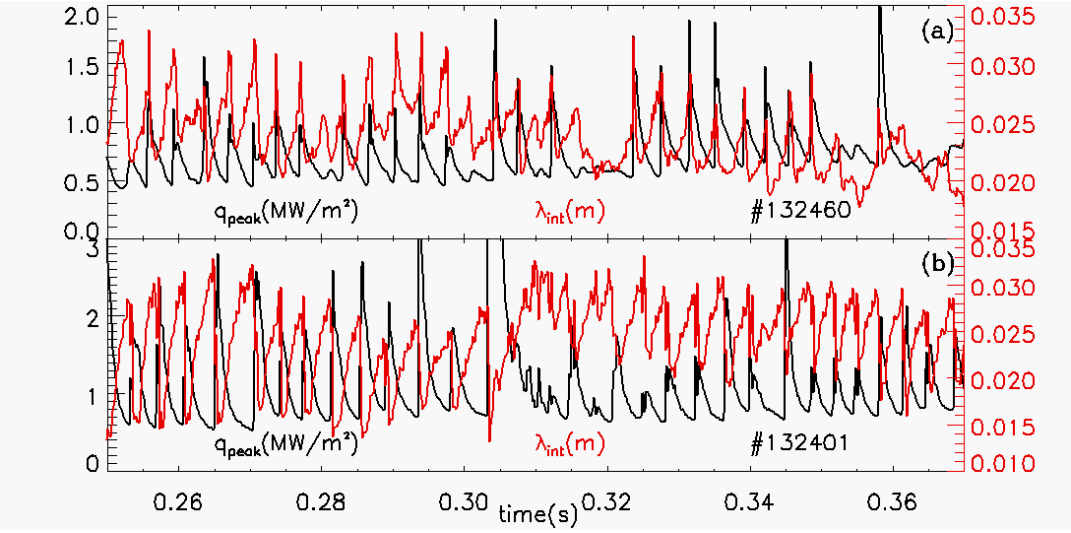

Figure 8

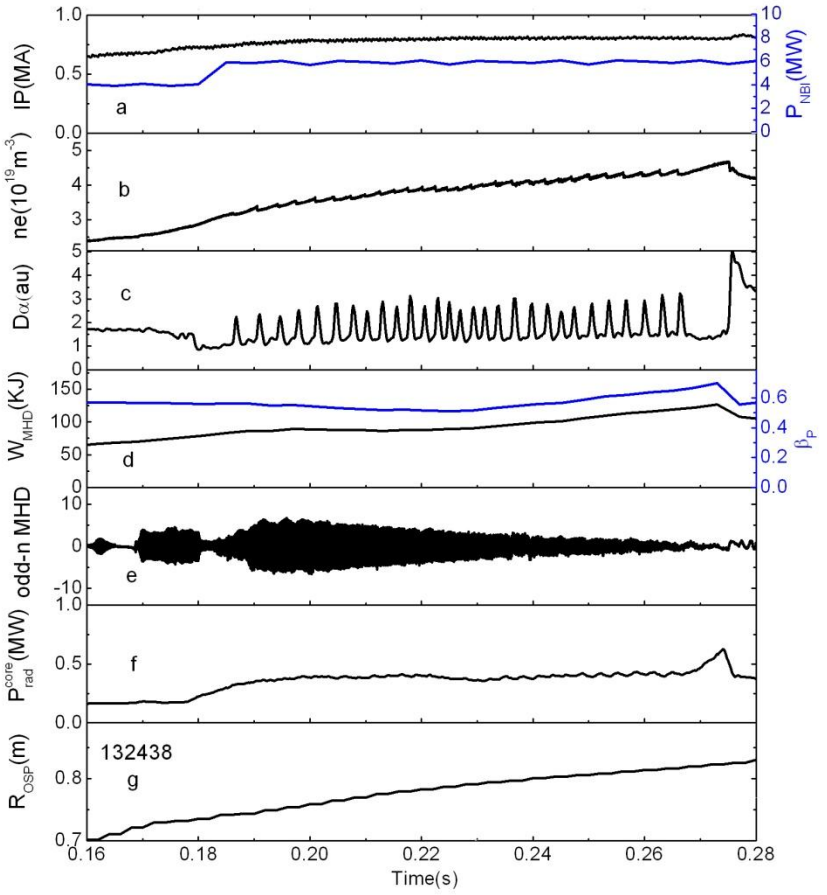
IP(MA)
P_{NBI}(MW)
ne($10^{19}m^{-3}$)
Dα(au)
W_{MHD}(KJ)
β_P
odd-n MHD
P_{rad}^{core}(MW)
R_{OSP}(m)
a
b
c
d
e
f
g
132438
Time(s)

Figure 9

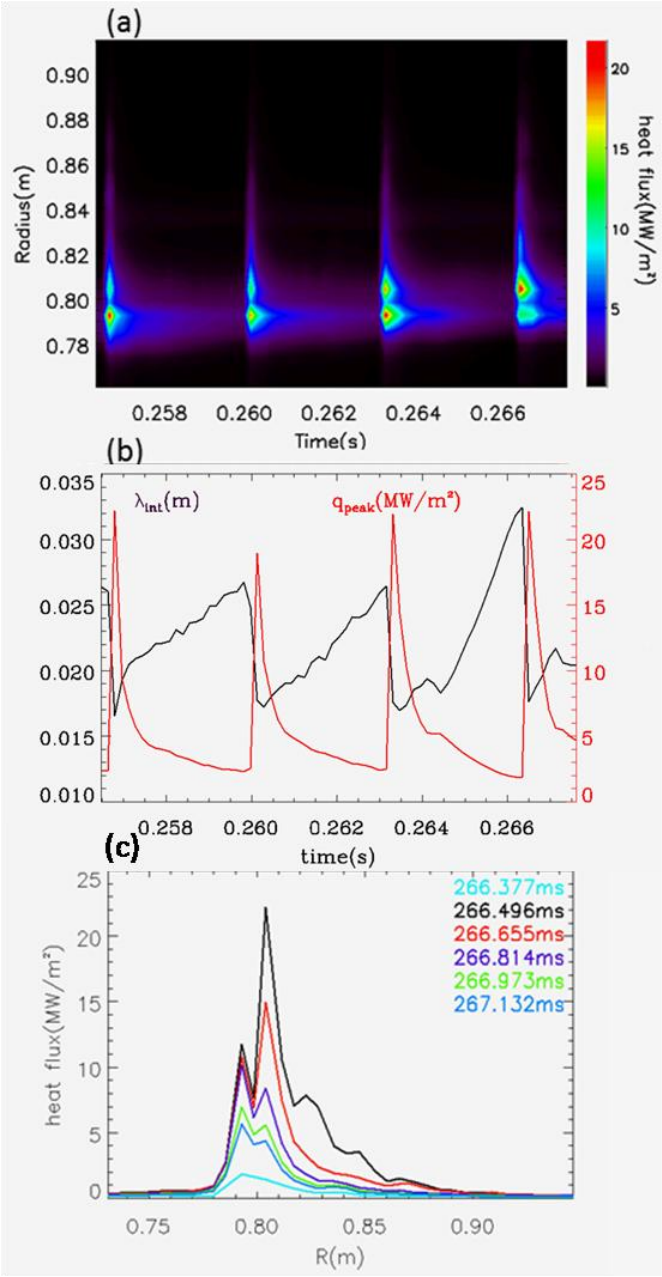
(a)
Radius(m)
0.90
0.88
0.86
0.84
0.82
0.80
0.78
0.258
0.260
0.262
0.264
0.266
Time(s)
heat flux(MW/m²)
20
15
10
5
(b)
λint(m)
qpeak(MW/m²)
0.035
0.030
0.025
0.020
0.015
0.010
25
20
15
10
5
0
0.258
0.260
0.262
0.264
0.266
time(s)
(c)
heat flux(MW/m²)
25
20
15
10
5
0
0.75
0.80
0.85
0.90
R(m)
266.377ms
266.496ms
266.655ms
266.814ms
266.973ms
267.132ms

Figure 10

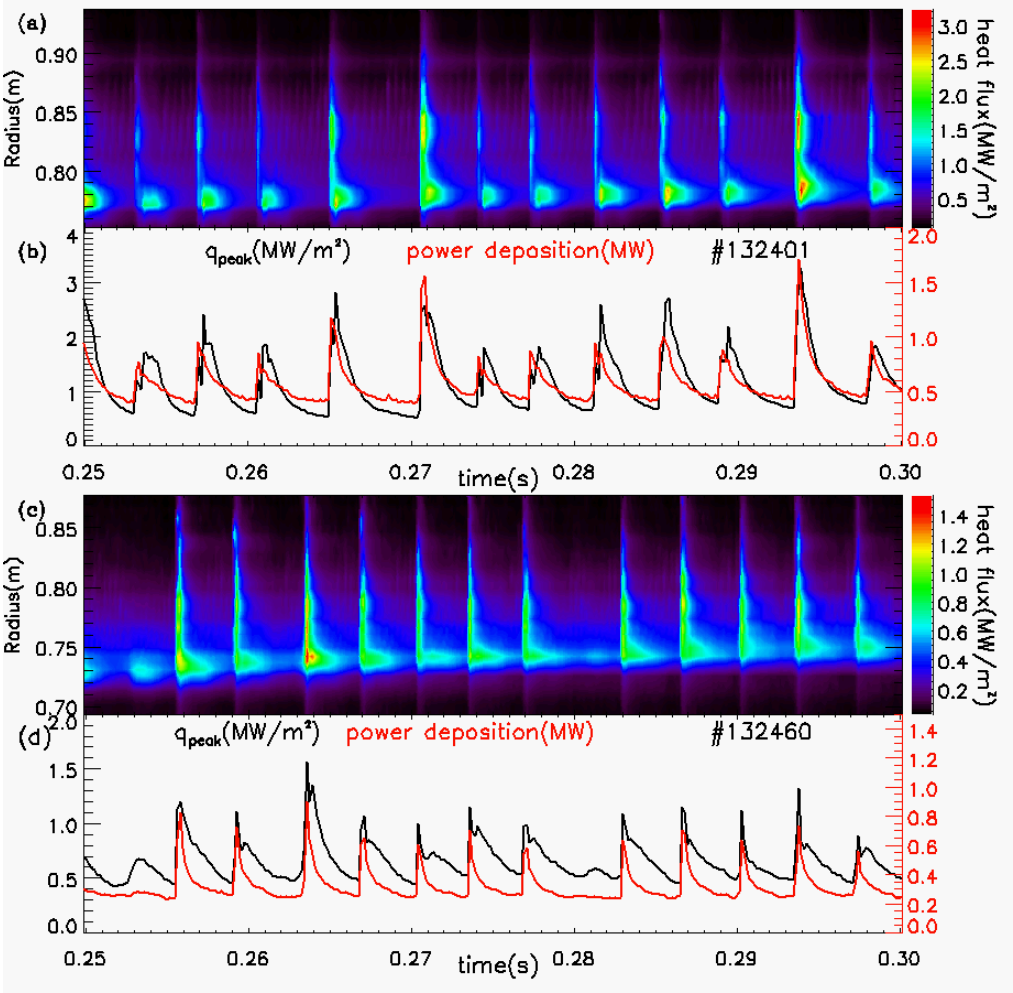
(a)
Radius(m)
0.90
0.85
0.80
heat flux(MW/m²)
3.0
2.5
2.0
1.5
1.0
0.5
(b)
q_peak(MW/m²)
power deposition(MW)
#132401
4
3
2
1
0
2.0
1.5
1.0
0.5
0.0
0.25
0.26
0.27
time(s)
0.28
0.29
0.30
(c)
Radius(m)
0.85
0.80
0.75
0.70
heat flux(MW/m²)
1.4
1.2
1.0
0.8
0.6
0.4
0.2
(d)
q_peak(MW/m²)
power deposition(MW)
#132460
2.0
1.5
1.0
0.5
0.0
1.4
1.2
1.0
0.8
0.6
0.4
0.2
0.0
0.25
0.26
0.27
time(s)
0.28
0.29
0.30

Figure 11

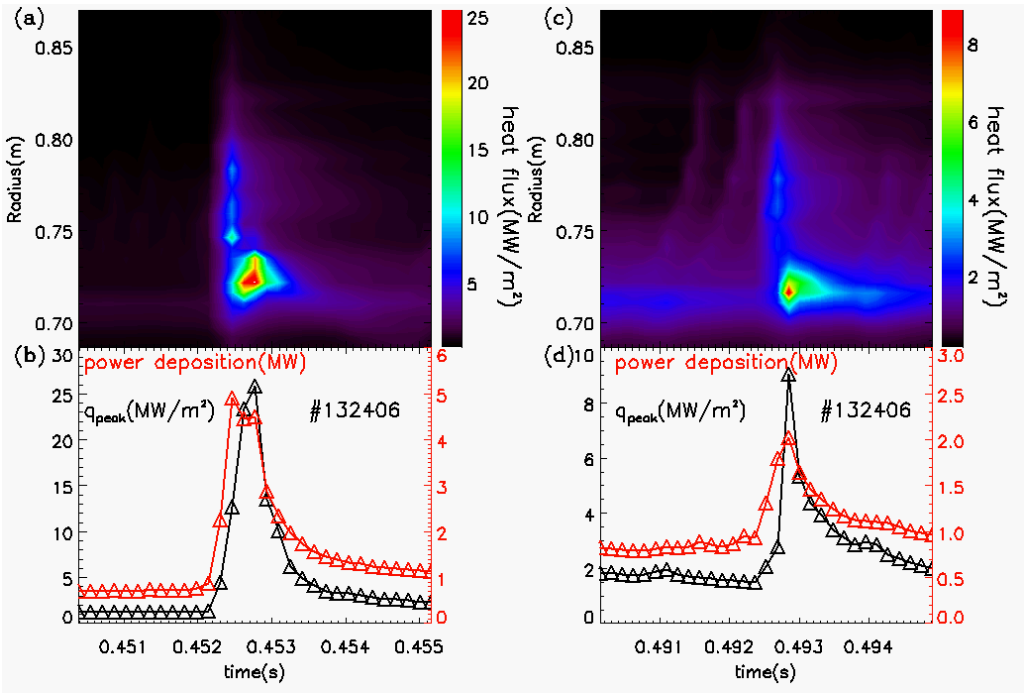
(a)
(b)
(c)
(d)
Radius(m)
heat flux(MW/m²)
power deposition(MW)
q_peak(MW/m²)
#132406
time(s)

Figure 12

References

1 *Kukushkin A. 2009 Nucl. Fusion 49 075008.*

2 *Wagner F., Becker G., Behringer K., et al. 1982 Phys. Rev. Lett. 49 1408.*

3 *Hill D. N. 1997 J. Nucl. Mater. 241-243 182.*

4 *Zohm H. 1996 Plasma Phys. Control. Fusion 38 105.*

5 *Hill D. N., A. Futch, A.W. Leonard, et al. 1992 J. Nucl. Mater. 196-198 204.*

6 Connor J. W., R.J. Hastie, H.R. Wilson, Miller R. L. 1998 *Phys. Plasmas* **5** 2687.

7 Snyder P. B., H. R. Wilson, J. R. Ferron*, et al.* 2002 *Phys. Plasmas* **9** 2037.

8 Wilson H. R., P.B. Snyder, G.T.A. Huysmans, Miller R. L. 2002 *Phys. Plasmas* **9** 1277.

9 Wilson H. R. and Cowley S. C. 2004 *Phys. Rev. Lett.* **92** 175006.

10 Kirk A., Koch B., Scannell R.*, et al.* 2006 *Phys. Rev. Lett.* **96** 185001.

11 Kirk A., Wilson H. R., Counsell G. F.*, et al.* 2004 *Phys. Rev. Lett.* **92** 245002.

12 Maqueda R. J., R. Maingi, NSTX team 2009 *Phys. Plasmas* **16** 056117.

13 Eich T., Herrmann A., Neuhauser J. 2003 *Phys. Rev. Lett.* **91**

14 Devaux S., Eich T., Arnoux G.*, et al.* 2011 *J. Nucl. Mater.* **415** S865.

15 Eich T., Herrmann A., Pautasso G.*, et al.* 2005 *J. Nucl. Mater.* **337-339** 669.

16 Maingi R., Bush C. E., Fredrickson E. D.*, et al.* 2005 *Nucl. Fusion* **45** 1066.

17 Maingi R., Sabbagh S. A., C.E. Bush*, et al.* 2005 *J. Nucl. Mater.* **337-339** 727.

18 Ono M., S.M. Kaye, Peng Y.-K. M.*, et al.* 2000 *Nucl. Fusion* **40** 557.

19 Fundamenski W., Eich T., Devaux S.*, et al.* 2011 *Nucl. Fusion* **51** 083028.

20 Jakubowski M. W., T.E. Evans, M.E. Fenstermacher 2009 *Nucl. Fusion* **49** 095013.

21 Maingi R., Bell M. G., Fredrickson E. D.*, et al.* 2006 *Phys. Plasmas* **13** 092510.

22 Maingi R., Tritz K., E. Fredrickson*, et al.* 2005 *Nucl. Fusion* **45** 264.

23 Loarte A., S. Bosch, A. Chankin*, et al.* 1999 *J. Nucl. Mater.* **266-269** 587.

24 Ahn J. W., R. Maingi, D.A. Mastrovito, Roquemore A. L. 2010 *Rev. Sci. Instrum.* **81** 023501.

25 Maingi R., Bell M. G., Bell R. E.*, et al.* 2003 *Plasma Phys. Control. Fusion* **45** 657.

26 Castle G. 1997 *COMPASS Note 97.16, UKAEA Fusion, Private Comm.*

27 E. Delchambre, G. Counsell and A. Kirk, Plasma Phys. Control. Fusion 51, 055012 (2009)

28 Gan K. F., J-W. Ahn, J.W. Park*, et al.* 2013 *Rev. Sci. Instrum*, 10.1063/1.4792595.

29 Herrmann A., W. Junker, K. Gunther*, et al.* 1995 *Plasma Phys. Control. Fusion* **37** 17.

30 Herrmann A. and team A.-U. 2001 *Proc. 28th EPS Conf. on Contr. Fusion and Plasma Physics, Madeira, Portugal, 18-22 June 2001* P5.104.

31 Sontag A. C., Canik J. M., Maingi R.*, et al.* 2011 *Nucl. Fusion* **51** 103022.

32 Sartori R. 2004 *Plasma Physics Controlled Fusion* **46** 723.

33 Maingi R., A.E. Hubbard, H. Meyer*, et al.* 2011 *Nucl. Fusion* **51** 063036.

34 Maqueda R. J., Wurden G. A., Zweben S.*, et al.* 2001 *Rev. Sci. Instrum.* **72** 931.

35 Zweben S. J., R.J. Maqueda, D.P. Stotler 2004 *Nucl. Fusion* **44** 134.

36 Lao L. L., H. St. John, R.D. Stambaugh*, et al.* 1985 *Nucl. Fusion* **25** 1611.

37 Sabbagh S. A., S.M. Kaye, J. Menard*, et al.* 2001 *Nucl. Fusion* **41** 1601.

38 Politzer P. A., Casper T., Forest C. B.*, et al.* 1994 *Phys. Plasmas* **1** 1545.

39 Leonard A. W., A. Herrmann, Itami K. 1999 *J. Nucl. Mater.* **266-269** 109.

40 Loarte A., G. Saibene, R. Sartori 2003 *Plasma Physics Controlled Fusion* **45** 1549.

41 Herrmann A. 2002 *Plasma Phys. Control. Fusion* **44** 883.

42 Gray T. K., R. Maingi, V.A. Soukhanovskii*, et al.* 2011 *J. Nucl. Mater.* **415** S360.

PPPL PRINCETON PLASMA PHYSICS LABORATORY

Princeton Plasma Physics Laboratory
Office of Reports and Publications

Managed by
Princeton University

under contract with the
U.S. Department of Energy
(DE-AC02-09CH11466)

P.O. Box 451, Princeton, NJ 08543
Phone: 609-243-2245
Fax: 609-243-2751

E-mail: publications@pppl.gov

Website: http://www.pppl.gov